

Formation of CaCO_3 hollow microspheres in carbonated distiller waste from Solvay soda ash plants

Wenjiao Xu, Huaigang Cheng (✉), Enze Li, Zihe Pan, Fangqin Cheng (✉)

Institute of Resources and Environmental Engineering, Engineering Research Center of CO_2 Emission Reduction and Resource Utilization, Ministry of Education of the People's Republic of China, Shanxi University, Taiyuan 030006, China

© Higher Education Press 2022

Abstract For decades, distiller waste and CO_2 were not the first choice for production of high valued products. Here, CaCO_3 hollow microspheres, a high-value product was synthesized from such a reaction system. The synthetic methods, the formation mechanism and operational cost were discussed. When $2.5 \text{ L} \cdot \text{min}^{-1} \cdot \text{L}^{-1}$ CO_2 was flowed into distiller waste ($\text{pH} = 11.4$), spheres with 4–13 μm diameters and about 2 μm shell thickness were obtained. It is found that there is a transformation of CaCO_3 particles from solid-cubic nuclei to hollow spheres. Firstly, the $\text{Ca}(\text{OH})_2$ in the distiller waste stimulated the nucleation of calcite with a non-template effect and further maintained the calcite form and prevented the formation of vaterite. Therefore, in absence of auxiliaries, the formation of hollow structures mainly depended on the growth and aging of CaCO_3 . Studies on the crystal morphology and its changes during the growth process point to the inside–out Ostwald effect in the formation of hollow spheres. Change in chemical properties of the bulk solution caused changes in interfacial tension and interfacial energy, which promoted the morphological transformation of CaCO_3 particles from cubic calcite to spherical clusters. Finally, the flow process for absorption of CO_2 by distiller waste was designed and found profitable.

Keywords distiller waste, CO_2 , hollow microsphere, CaCO_3 , $\text{Ca}(\text{OH})_2$, inside–out Ostwald effect

1 Introduction

Distiller waste is industrial wastewater produced during the classic Solvay process [1]. The amount of distiller waste produced from the ammonia regeneration process is

more than 10 times the amount of soda ash produced [2]. The distiller waste contains mainly CaCl_2 ($90\text{--}120 \text{ g} \cdot \text{L}^{-1}$) and NaCl ($40\text{--}60 \text{ g} \cdot \text{L}^{-1}$) along with small amounts of $\text{Ca}(\text{OH})_2$ and $\text{NH}_3 \cdot \text{H}_2\text{O}$ and has pH of 11 ± 1 [3,4]. In recent years, the annual volume of distiller waste produced globally was hundreds of million cubic meters, which was environment unfriendly. For decades, the technology for treatment of distiller waste was uneconomical, due to its high treatment costs and low output. One of the methods to improve the economic viability of the process is to increase the value addition of the end products. Extraction of high-value products from the distiller waste makes processing of this wastewater worthwhile.

Ca^{2+} ions are the predominant cations present in distiller waste. Obviously, the utilization of Ca^{2+} is regarded as one of the keys to the high-value treatment of the distiller waste. To make full use of the Ca resource in the distiller waste, researchers usually convert Ca^{2+} ions into micro/nano calcite or vaterite (different polymorphs of CaCO_3) by adding carbonates [5,6], which also effectively treats the distiller waste in this process [7]. Meanwhile, the addition of carbonates in the reaction inevitably results in the introduction of new cationic impurities such as Na^+ and K^+ into the reaction system [8]. This is undesirable because the reaction and the product quality cannot be properly controlled.

When it comes to carbon sources that lack cationic impurities, CO_2 obtained from the industrial exhaust gas, is the foremost [9]. Generally, CO_2 in flue gas needs to be enriched when it is applied in industrial practice. In fact, for years CO_2 has been increasing considered as a carbon source in the preparation of CaCO_3 from distiller waste [10]. CO_2 can be absorbed by the mixture of distiller waste and white mud by multiphase flow crystallization [5], reactive extraction–crystallization [7,11], etc., where CaCO_3 cubes/spheres with an average particle size of 10–100 μm get precipitated. Furthermore, nano- CaCO_3 particles with average particle size of 50 nm can also be

Received January 28, 2022; accepted March 29, 2022

E-mails: chenghg@sxu.edu.cn (Cheng H.),
cfangqin@sxu.edu.cn (Cheng F.)

obtained [3] with process reinforcements, e.g., fixing of CO₂ in a rotating packed bed. In spite of this, most of above CaCO₃ products are solid structures and have ordinary economic value. In fact, synthesis of hollow spheres from distiller waste can improve the economic value of the process, since hollow spheres can be used in more advanced applications, such as catalysts, fillers for rubber and coating [12]. However, it is generally considered impossible to synthesize CaCO₃ hollow spheres from the distiller waste, since their syntheses usually requires precise control with essential auxiliaries (i.e., templates and additives). In most cases, the auxiliaries like surfactants and high polymers [13,14] provide the centers for physical adsorption [15,16], chemical reaction [17,18] or crystal growth [19,20]. Meanwhile for the reaction system of distiller waste to obtain such a refined reaction environment for precipitation CaCO₃ hollow spheres is difficult. Thus, the existing reaction process cannot be high value because the solid microspheres do not have the same economic value as the hollow ones. An important question that arises is whether hollow spheres can be produced in such a reaction system.

A few studies on similar simple systems seem to indirectly provide an answer for this question. CaCO₃ hollow microspheres could be synthesized by continuous bubbling of CO₂ gas into a CaCl₂ aqueous solution without any auxiliary [21–23]. In this system, higher initial pH and infrared interference resulted in the higher proportion of hollow spheres [24]. However, there is still very little information available on the mechanism of formation of the hollow spheres in such reaction systems. Inspired by the reaction results in CaCl₂ solution [24], it can be hypothesized that from the distiller waste CaCO₃ hollow microspheres can be produced, since these simple alkaline systems contain CO₂ and Ca²⁺ ions. We believe that in presence of CO₂ atmosphere, alkaline distiller waste can also produce the unique product without any auxiliaries, since their main chemical components are the same.

Based on the above hypothesis, a new idea was proposed in this work, wherein the distiller waste was used to absorb CO₂ for the synthesis of CaCO₃ hollow microspheres, without the use of any auxiliary. Furthermore, attempt was made to study the mechanism of formation of hollow microspheres by this reaction. The technology used in this study has the potential to extract high value products from distiller waste and improve the economical aspect of processing of wastewater.

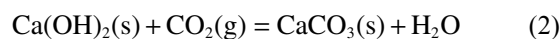
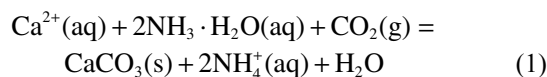
2 Experimental

2.1 Preparation of CaCO₃ hollow microspheres

CaCl₂ (analytical reagent ≥ 96%), NaCl (analytical

reagent ≥ 99.5%), and Ca(OH)₂ (analytical reagent ≥ 95%) were supplied by Sinopharm Chemical Reagent Co., Ltd., China. NH₃·H₂O (25–28 wt %) was purchased from Tianjin Hengxing Chemical Reagent Manufacturing Co., Ltd., China. The purity of CO₂ was 99.99%. Deionized (DI) water was obtained from Milli-Q, US.

Simulated distiller water was prepared from aqueous solutions of CaCl₂ (0.85–0.90 mol·L⁻¹), NaCl (0.86 mol·L⁻¹), Ca(OH)₂ (10.80 mmol·L⁻¹), and NH₃·H₂O (0.286 mol·L⁻¹). Then, 200 mL of the above solution was poured into in a 250 mL conical flask, and aerated with CO₂ (flow rate per unit feed liquid: 2.5 L·min⁻¹·L⁻¹) to start the continuous gas–liquid contact carbonation reaction. After the reaction, the CO₂ gas flow was discontinued and the solid products were separated from the reaction mixture by centrifugation at a speed of 10000 r·min⁻¹ for 10 min, and then they were washed twice with DI water. Finally, CaCO₃ hollow microspheres were obtained after drying in an oven at 60 °C. A schematic illustration of the experimental procedure is shown in Fig. 1 and the reaction formulae are shown in Eqs. (1) and (2),



2.2 Analysis methods

The morphologies of the obtained CaCO₃ products were determined by scanning electron microscopy (SEM; JEOL JSM-IT500HR, Japan, 5.0 kV; TM3030 145044-06, Japan, 15.0 kV). In addition, the elemental compositions of the samples were obtained by energy-dispersive X-ray spectroscopy (EDS; TM3030 145044-06, Japan, 15.0 kV). The morphological phases of the samples were determined by X-ray diffraction analysis (XRD; Bruker D2 Phaser, Germany) at the scan speed of 0.01(°)·s⁻¹ and a scan step of 0.1 s⁻¹ in the 2θ range of 10°–130°. Fourier transform infrared (FTIR) spectra were acquired on a FTIR Spectrometer (Thermo Scientific Nicolet iS50) at a resolution of 0.09 cm⁻¹. The samples were mixed with potassium bromide powder (2 mg sample in 300 mg KBr) and pelletized for analysis.

The concentrations of Ca²⁺ and Na⁺ ions in dilute aqueous solution were determined by inductively coupled plasma atomic emission spectroscopy (ICAP 6000, USA). Moreover, the solution pH during carbonation reaction was monitored using a pH meter (PHSJ-3F, China). The zeta potentials of the products were measured at 25 °C using a zeta potential and particle size analyzer (Malvern Zeta Sizer Nano-ZS90, UK). The values of θ and γ_{lg} of droplets were measured using powder contact angle meter (Krüss DSA25, Germany). The value of γ_{lg} was measured using pendant-drop method, whereas θ values between the crystal face of calcite and liquid phase were measured

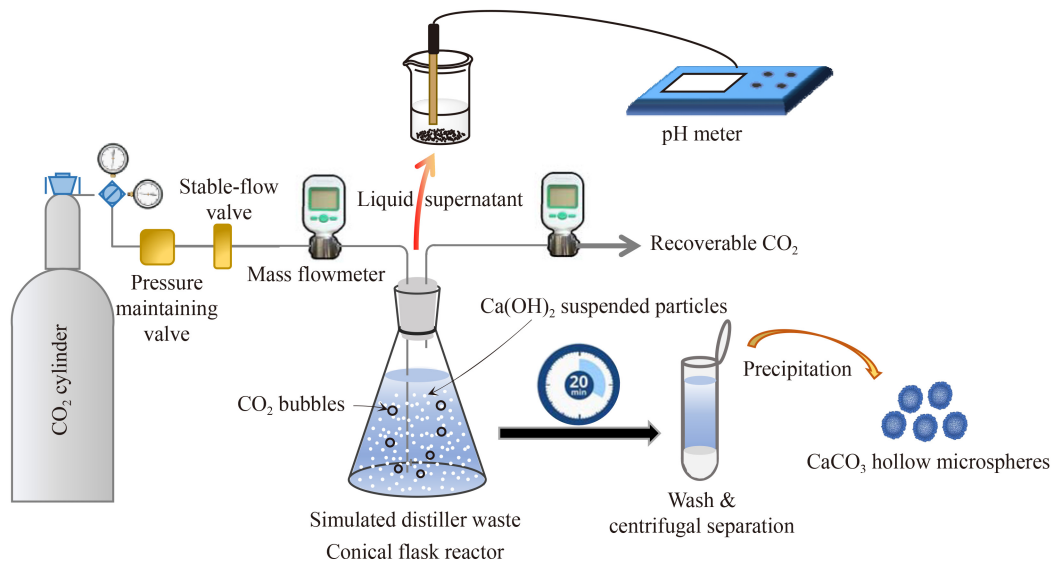


Fig. 1 Schematic illustration of the experimental procedure for the preparation of CaCO₃ hollow microspheres.

by the sessile-drop method. The crystalline faces of the exposed faces of calcite single crystals were analyzed by XRD (Crystal Products Factory Lianyungang, China).

2.3 Calculation methods

The different components of the polymorphs and their contents were determined from XRD peak intensities. The vaterite content of CaCO₃ polymorph was calculated from the corresponding characteristic peak intensities in the XRD pattern using Eqs. (3) and (4) [25,26]:

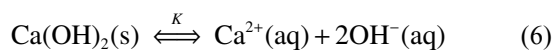
$$X_v = 7.69I_v^{110} / (7.69I_v^{110} + I_c^{104}), \quad (3)$$

$$X_c = 1 - X_v. \quad (4)$$

The total amount of CO₂ consumed during the carbonation reaction was calculated using Eq. (5):

$$V_{CO_2} = [(c_{Ca^{2+}} - c_{Ca^{2+}})V + n_{Ca(OH)_2}]V_m. \quad (5)$$

Applying Eq. (5) to the operation shown in Fig. 1, a total of about 3.25 L CO₂ can be fixed by 1 L distiller waste during the carbonation reaction. In the simulated distiller waste, presence of CaCl₂ and NH₃·H₂O would affect the solubility and dissociation equilibrium of Ca(OH)₂. The equilibrium for the dissociation reaction of Ca(OH)₂ is shown in Eq. (6). The formula for calculating the amount of undissolved Ca(OH)₂ (n) is represented by Eq. (7),



$$n = \frac{M \sqrt{K/\alpha_{Ca^{2+}}}}{2V}. \quad (7)$$

In contrast to its solubility in water at 20 °C (1.65 g·L⁻¹), Ca(OH)₂ can only dissolve only up to 0.072 g·L⁻¹ in this solution based on Eq. (7). Since the concentration of Ca(OH)₂ in distiller waste is 0.8 g·L⁻¹ (10.80 mmol·L⁻¹),

insoluble particles of Ca(OH)₂ in the distiller waste should be 0.728 g·L⁻¹, which would be dispersed forming a suspension.

The Pitzer model (the parameters and equations used in the Pitzer model are shown in Table S1 (cf. Electronic Supplementary Material, ESM) and Eqs. S(1)–S(20) (cf. ESM) was used to calculate the activity coefficients of Ca²⁺ ($\gamma_{Ca^{2+}}$) and OH⁻ (γ_{OH^-}) and the activity products (J) of Ca(OH)₂ at different moments were calculated using Eq. (8):

$$J = \alpha_{Ca^{2+}}(c_{OH^-})^2 = c_{Ca^{2+}}\gamma_{Ca^{2+}}(c_{OH^-}\gamma_{OH^-})^2, \quad (8)$$

γ_{ls} between the crystal face of calcite and the liquid phase was obtained from Young's calculation of Eq. (9):

$$\gamma_{ls} = \gamma_{lg} - \gamma_{sg}\cos\theta. \quad (9)$$

Herein, the interfacial phenomenon between calcite crystal and solution was studied by simulation of molecular dynamics (MD). The parameters and simulation process can be found in ESM, and calculation process and 3D schematic diagrams are shown in Fig. S1 (cf. ESM). θ values were also calculated using MD simulation, according to literature method [27] and these results were compared with the above experimental data. Finally, the averages of the measured and the calculated values were used in Eq. (9). Besides, the energies of calcite, solution, and system were calculated by MD simulations. Then, energies of the interactions were obtained and calculated according to Eq. (10). Here, the energy of the interaction was approximately the solid–liquid interfacial energy, since they were fairly consistent in their physical meaning,

$$\begin{aligned} \text{solid–liquid interfacial energy} &\approx \\ \text{the energy of the interaction} &= \\ \text{the energy of (calcite + solution – system)}. & \quad (10) \end{aligned}$$

The conversion ratio and output of CaCO₃ hollow

microspheres was calculated by using Eqs. (11) and (12):

$$\eta = (c_{\text{Ca}^{2+}} - c_{\text{Ca}^{2+}_{\text{min}}}) / c_{\text{Ca}^{2+}} \times 100\%, \quad (11)$$

$$Y = \eta T V M c_{\text{Ca}^{2+}} / 1000. \quad (12)$$

3 Results and discussion

3.1 Effect of $\text{Ca}(\text{OH})_2$ in distiller waste on the production of CaCO_3

In general the continuous introduction of CO_2 (Fig. 1) resulted in the continuous dissolution of suspended $\text{Ca}(\text{OH})_2$ particles in the distiller waste during the carbonation reaction, and SEM images and XRD patterns of the product are shown in Fig. 2. The solid particles formed at the beginning of reaction are shown in Fig. 2(a) and the final calcite-type hollow spherical clusters of 4–13 μm diameters are shown in Figs. 2(b) and 2(d(I)).

This suggested that the hollow structure was slowly obtained by transformation of the initially formed solid particles.

However, when the carbonation reaction was performed after $\text{Ca}(\text{OH})_2$ particles were filtered out from the distiller waste, spheres doped with vaterite and calcite could be observed instead of hollow spheres of pure calcite (Figs. 2(c) and 2(d(II))). The FTIR spectrum in Fig. 2(e) shows the peaks of vaterite (745 cm^{-1}) and calcite (712 cm^{-1}). The reason is the generation of metastable phases in the absence of $\text{Ca}(\text{OH})_2$ particles. According to Kelvin equation and Young–Laplace equation [28], the formation of solid crystals as a new phase in the clear solution is difficult, due to the lack of original nuclei (i.e., suspended $\text{Ca}(\text{OH})_2$ particles). This results in the significant increase in partial oversaturation of CaCO_3 coupled with the promotion of ammonia, which eventually leads to the formation of CaCO_3 crystals containing metastable vaterite (12.6%, according to Fig. 2(d(II))) [29,30]. Meanwhile, the presence of $\text{Ca}(\text{OH})_2$

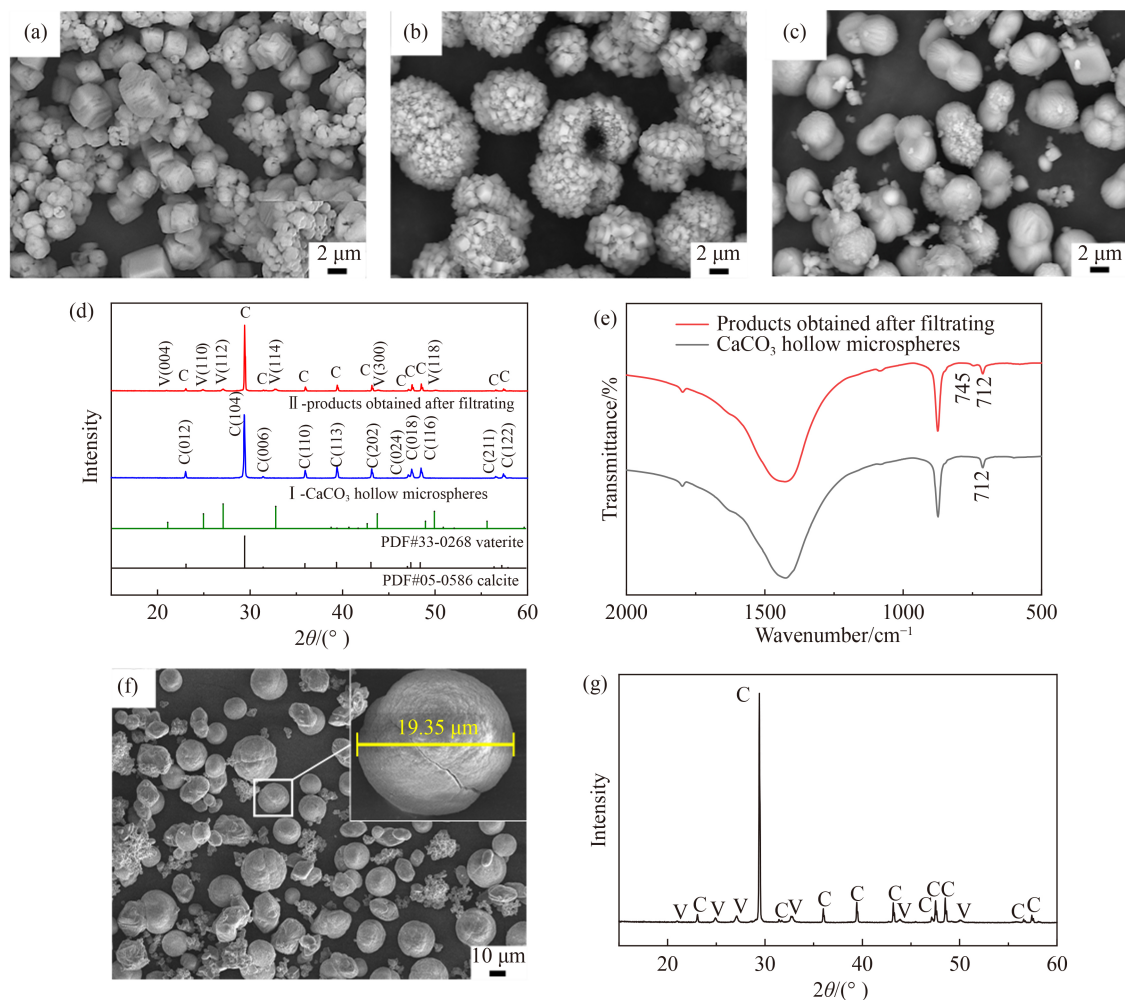


Fig. 2 SEM images of the carbonation products obtained from DI waste (a) reacted for 10 min, (b) reacted for 20 min, (c) after filtration reacted for 20 min; (d) and (e) are XRD patterns and FTIR spectra of samples (b) and (c), respectively (C: calcite; V: vaterite); (f) SEM image and (g) XRD pattern of the carbonation product when the Ca source in the distiller waste is only $\text{Ca}(\text{OH})_2$.

solids in the distiller waste prevents the above-mentioned situation, thus generating stable calcite crystals (Fig. 2(b)). This ensures that the presence of Ca(OH)₂ suspended particles contributes in a big way to the generation of hollow spheres.

There are two Ca sources in the distiller waste, i.e., Ca(OH)₂ and CaCl₂. When the Ca source in the distiller waste is only Ca(OH)₂, solid and spherical CaCO₃ with about 20 μm in diameter appeared in the product, and 15.3% of them were verified to be vaterite, as shown in Figs. 2(f) and 2(g). Since Ca(OH)₂ is slightly soluble in water, the Ca²⁺ in the system is much lower than that of the distiller waste. This leads to the increase of ammonia-calcium ratio, which promotes the formation of solid spherical vaterite [31]. This phenomenon indicates that sufficient Ca source to prepare CaCO₃ hollow microspheres has to be provided by CaCl₂. Therefore, besides Ca(OH)₂, CaCl₂ also plays a key role in the formation of hollow spheres.

As shown in Fig. 3, taking into account the changes in Ca²⁺ ion concentration (Fig. 3(a)) and pH (Fig. 3(b)) during the reaction, the carbonation of Ca(OH)₂ was further analyzed on the basis of ion activity of the multi-system, as shown in Table 1. Results of calculation showed that both $\gamma_{\text{Ca}^{2+}}$ and γ_{OH^-} dropped sharply once the time CO₂ was introduced. Especially, $\gamma_{\text{Ca}^{2+}}$ decreased from

1.2 to 0.3 (closer to the similar systems [32,33]), causing J of Ca(OH)₂ to drop from 9.36×10^{-6} to 5.42×10^{-6} , which was smaller than K (5.6×10^{-6}) [34]. Therefore, as long as CO₂ was introduced, the tendency of dissolution of the suspended Ca(OH)₂ particles increased. Hence, Ca(OH)₂ particles dissolved and rapidly reacted with CO₂. Therefore, the calcite formed by the reaction of Ca(OH)₂ and CO₂ is the nucleus for the growth of CaCO₃ hollow microspheres, not the Ca(OH)₂ particles. The samples showed core-shell hollow morphologies after reaction for 20 min, as shown in Fig. 4. EDS analysis shows uniform distribution of Ca, C, and O elements in both the core and shell, which indicated that the structure did not have an inner Ca(OH)₂ core and outer CaCO₃ shell, as shown in Figs. 4(a-c). This implied that the original Ca(OH)₂ particles already started disappearing as CaCO₃ hollow spheres were growing. Therefore, the subsequent growth of hollow microspheres relied more on the CaCO₃ aging than the induction of Ca(OH)₂.

It was found that the size of suspended Ca(OH)₂ would affect the formation of CaCO₃ hollow structures, e.g., the carbonation products generated from the large Ca(OH)₂ particles (≈ 12 μm, as shown in Fig. 4(d)) were fusiform CaCO₃ with solid structures (as shown in Fig. 4(e)), unlike the hollow ones prepared by small Ca(OH)₂ particles (roughly < 3 μm, as shown in Figs. 4(f) and

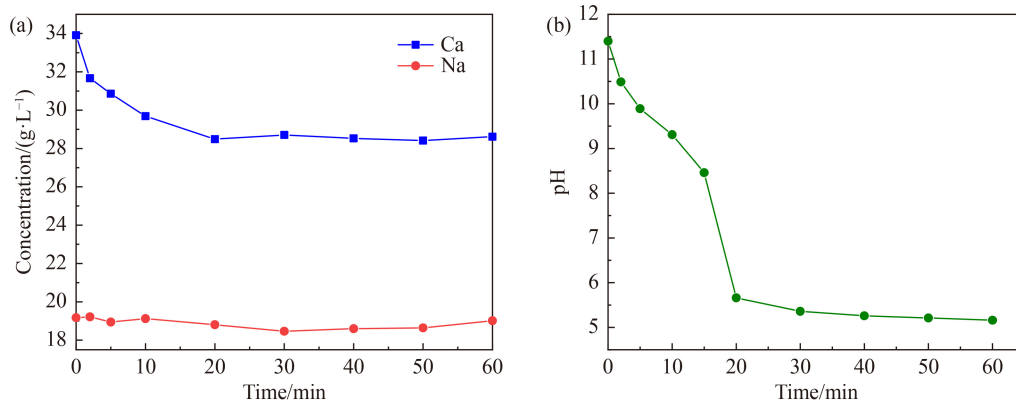


Fig. 3 (a) Curves of changes in Ca²⁺ and Na⁺ ion concentrations in solution with reaction time, and (b) curves showing changes in pH of the reaction system with reaction time.

Table 1 Experimental values of $c_{\text{Ca}^{2+}}$ and c_{OH^-} , calculated values of $\gamma_{\text{Ca}^{2+}}$, γ_{OH^-} , $\alpha_{\text{Ca}^{2+}}$, α_{OH^-} , and J

Reaction time/min	pH of solution	Concentration/(mol·L ⁻¹)		Coefficient activity		Activity/(mol·L ⁻¹)		J
		$c_{\text{Ca}^{2+}}$	c_{OH^-}	$\gamma_{\text{Ca}^{2+}}$	γ_{OH^-}	$\alpha_{\text{Ca}^{2+}}$	α_{OH^-}	
0 ^{a)}	11.4	0.85	2.51×10^{-3}	1.19826	1.2079	1.018521	3.03×10^{-3}	9.36×10^{-6}
0 ^{b)}	11.4	0.85	2.51×10^{-3}	0.30722	0.728888	0.261137	1.83×10^{-3}	5.42×10^{-6}
2	10.49	0.79	3.09×10^{-4}	0.19488	0.652078	0.1539552	2.01×10^{-4}	1.82×10^{-8}
5	9.89	0.77	7.76×10^{-5}	0.172587	0.634418	0.13289199	4.92×10^{-5}	9.20×10^{-10}
10	9.31	0.74	2.04×10^{-5}	0.146964	0.612986	0.10875336	1.25×10^{-5}	4.80×10^{-11}
15	8.46	0.72	2.88×10^{-6}	0.133638	0.601384	0.09621936	1.73×10^{-6}	8.13×10^{-13}
20	5.66	0.71	4.57×10^{-9}	0.127701	0.596131	0.09066771	2.72×10^{-9}	1.90×10^{-18}
60	5.16	0.71	1.45×10^{-9}	0.127701	0.596131	0.09066771	8.64×10^{-10}	1.85×10^{-19}

a) Before CO₂ was passed into the distiller waste; (b) after CO₂ was passed into the distiller waste, there were CO₃²⁻ in the system.

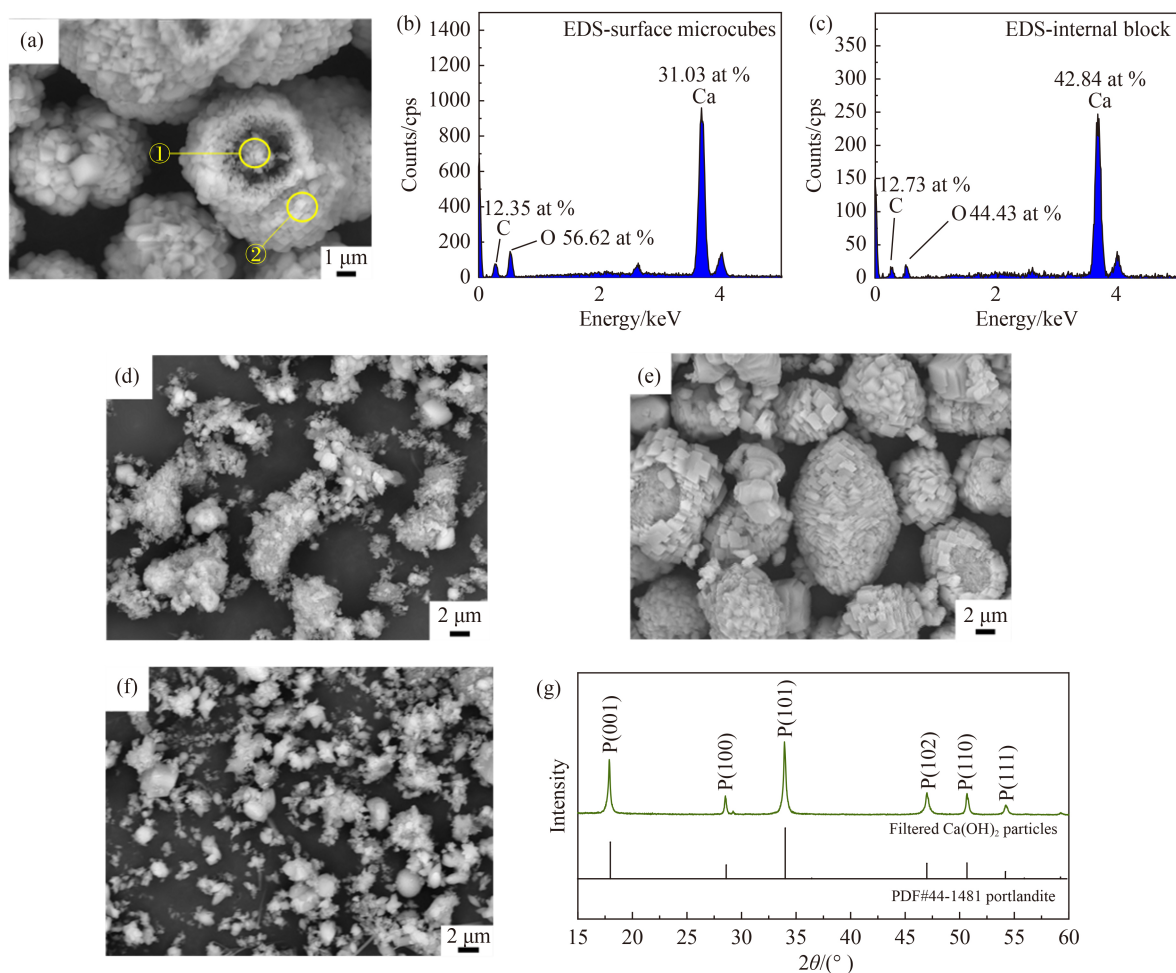


Fig. 4 (a) SEM image of a sample with a core-shell morphology; (b) and (c) EDS analyses of points (1) and (2), respectively, from part (a); SEM images of (d) the $\text{Ca}(\text{OH})_2$ particles filtered from distiller waste after a period of agglomeration and growth; (e) the product obtained from distiller waste after $\text{Ca}(\text{OH})_2$ particles has been agglomerated and grown for a period; (f) SEM image of $\text{Ca}(\text{OH})_2$ particles filtered from distiller waste; (g) XRD pattern of $\text{Ca}(\text{OH})_2$ particles filtered from distiller waste (P: portlandite).

4(g)). However, it is worth pointing out that the products from the fresh distiller waste should still be hollow CaCO_3 microspheres (as shown in Fig. 2(b)) in most cases, because large $\text{Ca}(\text{OH})_2$ particles would not exist unless there is sufficient period of agglomeration and growth. Furthermore, after the filtration of $\text{Ca}(\text{OH})_2$ particles from the fresh distiller waste and vacuum drying, both the size distribution and the shape of $\text{Ca}(\text{OH})_2$ which had been verified in its phase structure were found irregular, as shown in the Fig. 4(f). In other words, neither the size distribution nor the shape of $\text{Ca}(\text{OH})_2$ particles was consistent with those of the generated CaCO_3 hollow spheres in Fig. 2(b). This pointed out to an impossibility of $\text{Ca}(\text{OH})_2$ particles acting as templates for the growth of CaCO_3 hollow spheres. Thus, the suspended $\text{Ca}(\text{OH})_2$ particles play an important effect on CaCO_3 morphology, but not the template effect.

Comprehensively, based on Figs. 2–4, it was evident that the role of $\text{Ca}(\text{OH})_2$ in the reaction was to provide an initial crystal nucleus to stimulate the formation of calcite

particles. Then, the $\text{Ca}(\text{OH})_2$ dissolved and disappeared by itself to leave a hollow structure that was further refined during the growth of CaCO_3 . This also meant that at least the growth stage of hollow microspheres was an auxiliary-free system.

3.2 Formation of CaCO_3 hollow microspheres

The formation of CaCO_3 hollow microspheres is shown in Figs. 5 and 6. XRD spectrum showed that there are only characteristic peaks of calcite in Fig. 6(a). In the FTIR spectrum of Fig. 6(b), 1798 cm^{-1} is the stretching vibration peak of $\text{C}=\text{O}$, 1432 cm^{-1} is the antisymmetric stretching vibration peak of CO_3^{2-} , and the characteristic peaks of calcite are at 845 cm^{-1} (the out-of-plane bending vibration peak of calcite CO_3^{2-}) and 712 cm^{-1} (the in-plane bending vibration peak of CO_3^{2-}). Thus, XRD and FTIR analyses showed that CaCO_3 was always present in calcite form throughout the process. Moreover, the explanations of the formation process of the hollow microspheres were shown in Fig. 7. The first 10 min of

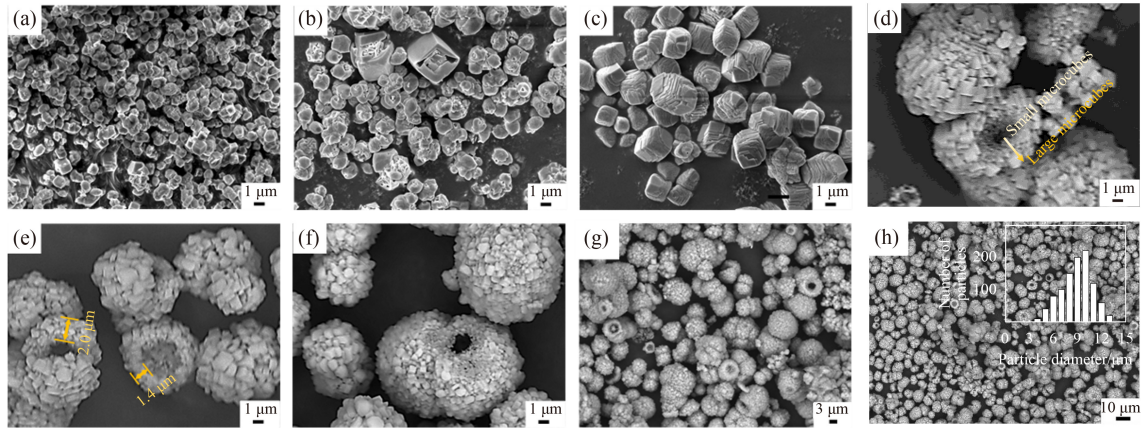


Fig. 5 SEM images of samples obtained by carbonization reaction at different times: (a) 2 min, (b) 5 min, (c) 10 min, (d) 15 min, (e) 20 min, and (f) 60 min; (g) and (h) show hollow microspheres at lower magnification (reaction time of 20 min); the inset of (h) shows the diameter distribution of the particles.

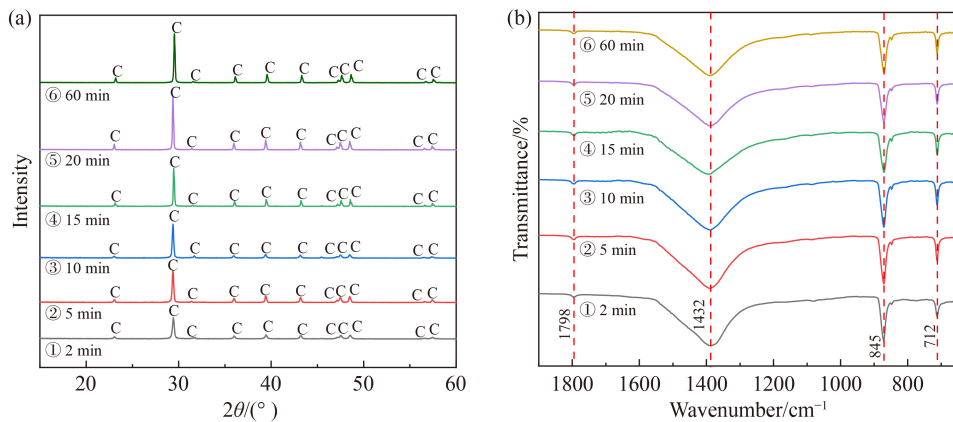


Fig. 6 (a) XRD patterns and (b) FTIR spectra of carbonization products in Figs. 5(a–f), respectively.

carbonation process involves the nucleation to growth of solid structural calcite, as shown in Figs. 5(a–c) and 7(a(1)) and 7(b(1)). The square particles would then transform into preliminarily spherical shape due to the interfacial properties, as shown in Figs. 5(d), 7(a(2)) and 7(b(2)). The key to finally forming hollow microspheres lies in the third step. As for step (3), there are two potential explanations for the formation mechanism of hollow microspheres in an auxiliary-free system: Ostwald ripening and Kirkendall effect [35].

From Fig. 5(d) it was clear that the outer microcubes were larger than the inner microcubes during the formation of hollow microsphere. According to the inside–out Ostwald ripening mechanism [36,37], the smaller microcubes inside the spheres have higher surface energy and larger curvature. This makes it more soluble compared with the microcubes on the outer layer, which leads to the gradual dissolution of the inner particles [38]. The internal cavity is formed and gradually expands until a complete hollow sphere is generated. Meanwhile, core–shell intermediates with hollow interiors [39] are generated (as shown in Fig. 4(a)). The above mechanism of inside–out Ostwald ripening process is represented in

Fig. 7(a).

Secondly, since there are two different Ca sources in distiller waste, i.e., Ca(OH)₂ particles and Ca²⁺ ions in the solution, the calcite produced by these two sources of Ca could form homogeneous-heterotopic interfaces. According to the Kirkendall effect [40–42], the defect sites developed at the homogeneous-heterotopic interface merge at the boundary, forming the core–shell intermediates with hollow interiors. Differences in the mass diffusion rates result in net outward mass flow from the core to shell, leaving defects to collect into cavities [43]. The mechanism of entire process based on interior Kirkendall effect is shown in Fig. 7(b).

Mass transfer occurs on the particle surface during the Ostwald ripening process, which is different from the Kirkendall process. From Fig. 8, it can be seen that the formation of hollow microspheres gets disturbed or destroyed (as shown in Fig. 8(a)) when the bulk of the reaction fluid is stirred, which is an indirect conformation of occurrence of mass transfer on the particle surface of calcite (as shown in Fig. 8(b)). Combining this fact and Fig. 5(d) showed that the Ostwald effect was more convincing for explaining the formation of the hollow

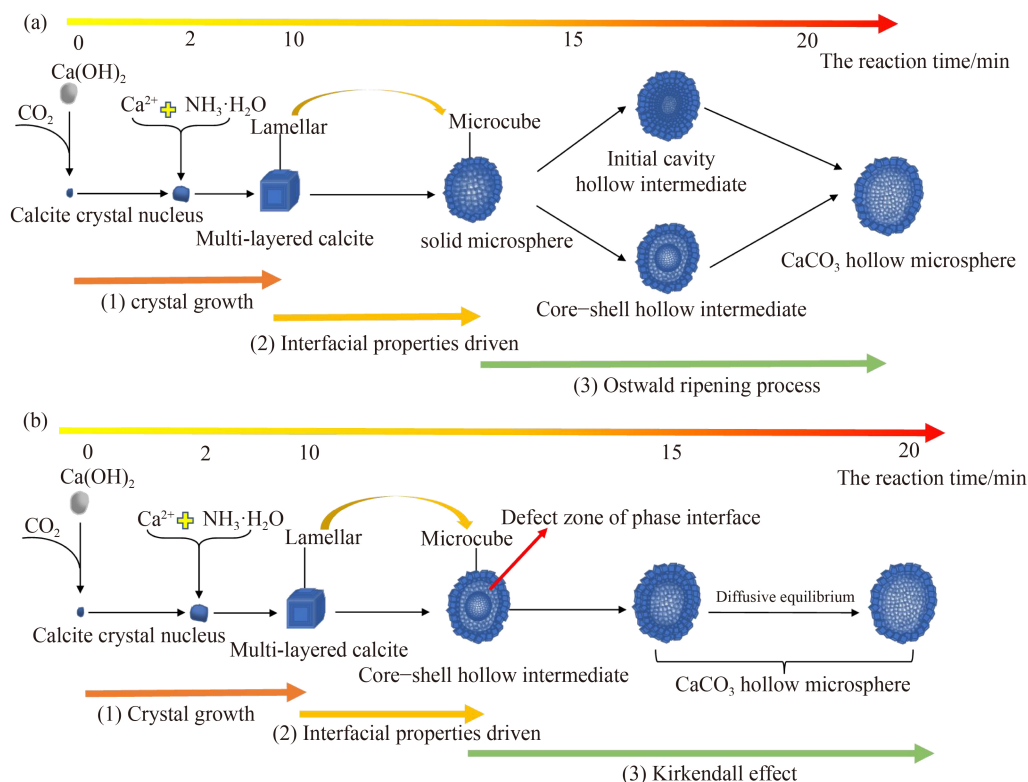


Fig. 7 Scheme showing the two potential explanations for the formation mechanism of CaCO₃ hollow microspheres: (a) Ostwald ripening and (b) Kirkendall effect.

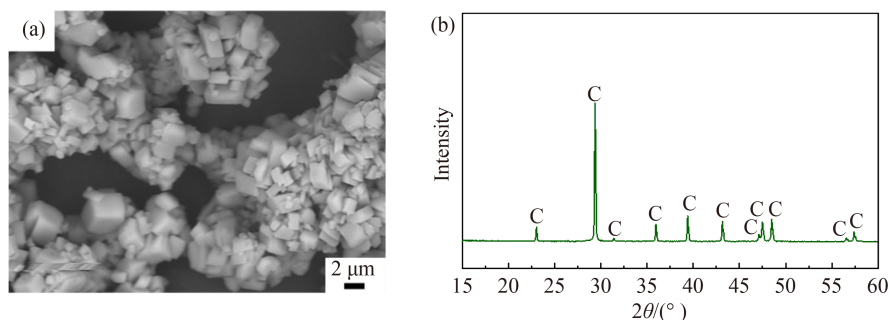


Fig. 8 (a) SEM image of the product obtained by carbonation reaction under magnetic stirring; (b) XRD pattern of products of carbonization reaction under stirring.

structure.

As shown in Figs. 5(e) and 5(f), the CaCO₃ hollow microspheres of about 2 μm shell thickness were produced in 20 min, and there was no significant change till 60 min. Figures 5(g) and 5(h) provide a better view of the size distribution of hollow balls at low magnification. The size range of spheres was 4–13 μm and the average size was about 9 μm, as shown in the inset in Fig. 5(h).

3.3 Interfacial properties driven the morphology transition

The above discussion explains the process for nucleation of calcite crystal (Figs. 5(a–c)) and formation of CaCO₃ hollow spheres (Figs. 5(d–f)) but does not explain the transformation from solid block structure into spherical microcube clusters (Fig. 5(c) to Fig. 5(d) and step (2) in

Fig. 7(a)). It is well known that interfacial properties have a significant impact on the recharging of microparticles or aggregates [44]. Obviously, the morphological transition shown in Fig. 7(a(2)) is co-related to the interfacial properties, including interfacial tension and interfacial energy.

The interfacial properties on the face (104) of calcite specimen were assessed, because it has been proven to be the main crystal face of CaCO₃ hollow spheres, as shown in Fig. 6(a). The stability and exposure of face (104) have also been supported by previous studies [45–47]. The XRD pattern of face (104) of the CaCO₃ specimen is shown in Fig. S2 (cf. ESM). Moreover, the interfacial tension was determined. As the carbonation reaction progressed, there was a constant change in the composition of bulk liquid. According to Young's Eq.

(9), the values of θ , γ_{lg} , and γ_{ls} obtained between the face (104) of calcite and the liquid phase at different reaction times are shown in Table 2. In addition, γ_{sg} can be considered to remain constant at 43.5 mN·m⁻¹ [48]. The results pointed to a decreasing–increasing trend of γ_{ls} during the carbonation reaction. Specifically, in the first 10 min of the reaction, the surface tension dropped by 4.4 mN·m⁻¹, whereas in the next 10 min, it rose by 2.7 mN·m⁻¹. This trend was consistent with the changes in pH of liquid phase in Fig. 3(b). This suggested that the changes in the chemical properties of the bulk solution caused changes in interfacial tension between solid and liquid phase, and then indirectly caused changes in the interfacial properties and then affect the crystal growth–assembly, followed by the morphology transition in the crystal growth process. This led to a transition from cubic morphology to spherical polymorph of the particles with no change in the solid face (104).

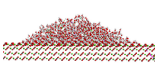
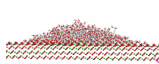
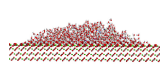
The interfacial tension of a solid has the contribution of two factors: one is the contribution of the interfacial energy, and the other is contributed by the change in interfacial energy due to the changes in surface area. On one hand, as for the former, the interfacial energy of the crystal during the changes in liquid phase was roughly calculated by MD simulation, as shown in Fig. 9. The examples of simulation of calcite cell surfaces of system are shown in Figs. 9(a–c). As shown in Table S2 (cf. ESM) and Fig. 9(d), the interfacial energy decreased by 62.85 kcal·mol⁻¹ from the start of the reaction up to 10 min (from the nucleation to the growth of calcite). The next 10 min of the process involved the transformation of calcite from multilayer blocks to hollow microspheres and the interfacial energy decreased by 14.71 kcal·mol⁻¹. From the nucleation to the growth of CaCO₃ hollow microspheres, the slight decrease in interfacial energy

reflected the transition of the system to a more stable state. On the other hand, for the change in interfacial energy caused by the changes in surface area (the latter), it is the difference between the interfacial tension (Table 2) and energy (Table S2) [49]. The changing trend of these differences is shown in Fig. 9(d), where it increased from 10 to 20 min of reaction. This corresponded to the obvious changes in the surface structure of the product, i.e., the surface lamellae of block calcite are transformed into microcube surfaces of hollow spheres (with the inner and outer surfaces, hollow spheres have larger surface area). Therefore, changes in the interfacial properties can be regarded as one of the reasons for the transformation of the main structure and building unit of the product [50]. This is also induced by the changes in physico-chemical properties of liquid phase, e.g., change in pH value.

3.4 Flow diagram of the process and operational cost analysis

Based on the experimental procedures for the preparation of CaCO₃ hollow microspheres by absorption of CO₂ into the distiller waste, the technical flow diagram of the process was designed as shown in Fig. 10. Based on the carbon sequestration efficiency of 1 ton distiller waste (about 90% in the total operation cycles), the flow rate of CO₂ was calculated. Mother liquor and process gas (CO₂) were considered to be circulating in the process shown in Fig. 10. It was assumed that they circulated 5 times, followed by discharge of certain amount of tail mother liquor and tail gas. It was empirically assumed that the total conversion ratio of Ca²⁺ could eventually reach 90% in this flow process based on the Eqs. (11) and (12) [51]. The additionally supplemented industrial ammonia and

Table 2 The average of multiple tests, MD simulation results and images of θ , the average value of γ_{lg} from multiple tests, as well as the calculated values of γ_{ls} between the crystal face (104) of calcite and water/solution at different reaction times

Liquid value		Water	Distiller waste	The solution after reaction for		
				5 min	10 min	20 min
$\theta/(^\circ)$	Test value	28.5	37.2	33.7	28.2	32.0
						
	MD simulation results ^{a)}	–		–		
		73.43	69.25	67.73	68.50	69.78
	$\gamma_{lg}/(\text{mN}\cdot\text{m}^{-1})$					
	$\gamma_{ls}/(\text{mN}\cdot\text{m}^{-1})$ calc.	35.27	34.60	31.53	30.16	32.81

a) The method for contact angle measurement in MD can be found in literature [27].

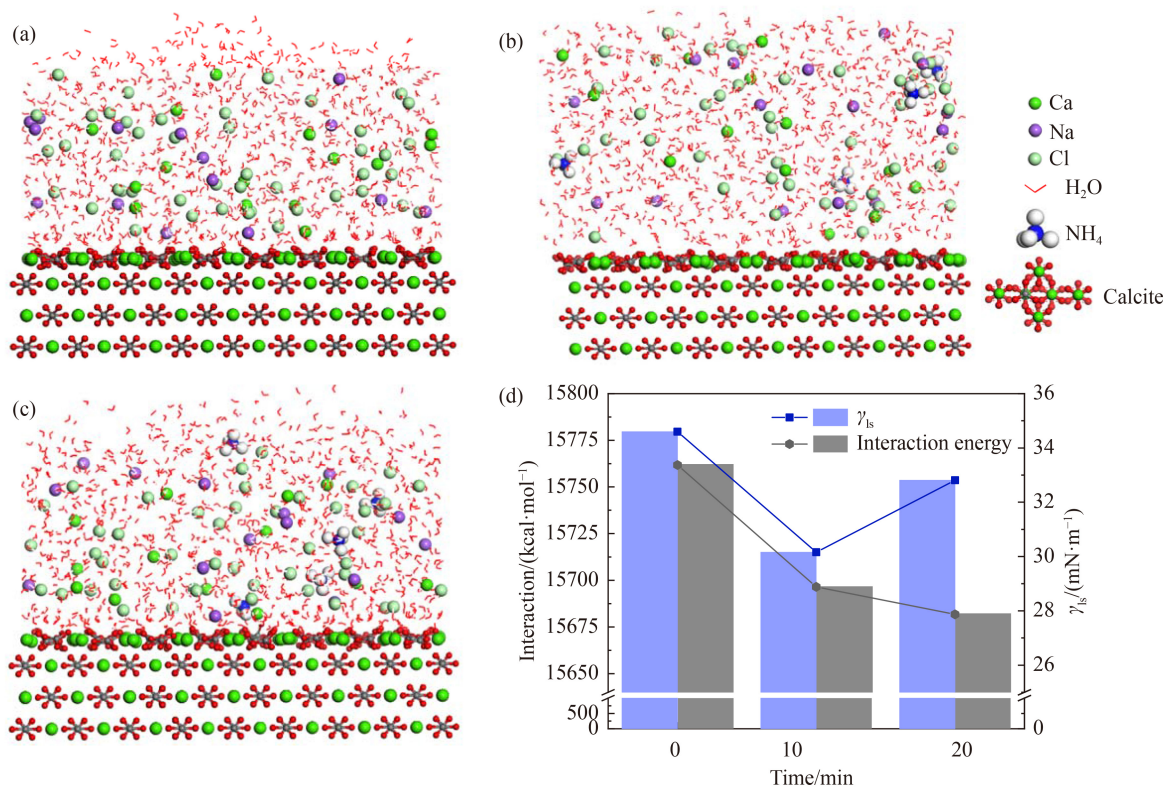


Fig. 9 Examples of simulation of calcite cell surface (the (104) surface is exposed to the liquid layer) of system after reacting for (a) 0 min, (b) 10 min, and (c) 20 min; (d) the diagram of interfacial energy and tension between calcite and liquid phase with reaction time.

milk of lime could maintain the alkaline conditions of the mother liquor, and the supplemented $\text{Ca}(\text{OH})_2$ particles could induce the production of hollow spheres. It should be mentioned that the low concentration of CO_2 can prevent the formation of spherical CaCO_3 particles [31], the detailed analysis as shown in Fig. S3 (cf. ESM), so in practice, the low-concentration CO_2 in the flue gas should be enriched (e.g., by alkanolamine absorbent) before reacting with aqueous Ca^{2+} .

In addition, the operational cost of the process was evaluated, as shown in Table 3. Processing 1 ton distiller waste per hour would require about 85 vol % flue gas 4.5 $\text{m}^3 \cdot \text{h}^{-1}$, 25 wt % waste ammonia 20 $\text{L} \cdot \text{h}^{-1}$, and 80 wt % milk of lime 1 $\text{kg} \cdot \text{h}^{-1}$. Moreover, the energy consumption of fluid flow was roughly neglected and the energy consumption of latent heat of evaporation was not involved in the process, resulting in overall less energy consumption. The total cost was CNY 40.2 per ton distiller waste and mainly the yield of CaCO_3 hollow microsphere was considered. The market price of CaCO_3 is in the range of CNY 300 to CNY 2000. Considering that the CaCO_3 hollow microspheres were relatively uniform in this work, the economic estimate was made based on the product price of CNY 1500 per ton. Eighty kg of CaCO_3 hollow microspheres are produced from every ton of distiller waste and the yield is estimated to be CNY 120. In total, the profit generated from 1 ton distiller waste is CNY 79.8, as shown in Table 4.

However, equipment cost and its maintenance, as well as public works and other expenses generally account for more than half of the total operating cost [52]. Thus, the profit from this process can be considered as half, i.e., it can be estimated that CNY 39.9 per ton distiller waste would be the final operational profit. In summary, the process is operationally feasible.

4 Conclusions

The co-processing of distiller waste and CO_2 gas was explored, wherein simulated distiller waste was used for CO_2 fixation. CaCO_3 hollow microspheres were obtained by precipitation, which were 4–13 μm in diameter and about 2 μm in shell thickness. Results showed that CaCO_3 particles transformed from solid-cubic nuclei to hollow spheres. Firstly, the $\text{Ca}(\text{OH})_2$ particles in the distiller waste did not act as templates for hollow spheres, but induced the formation of calcite nuclei. This led to presence of CaCO_3 particles in the form of calcite from the beginning and prevented the formation of metastable vaterite. In such an auxiliary-free system, the formation of hollow spheres occurred mainly through the growth and aging of CaCO_3 particles themselves. Based on the crystal morphology and its changes during the growth process, it was deduced that Ostwald ripening could

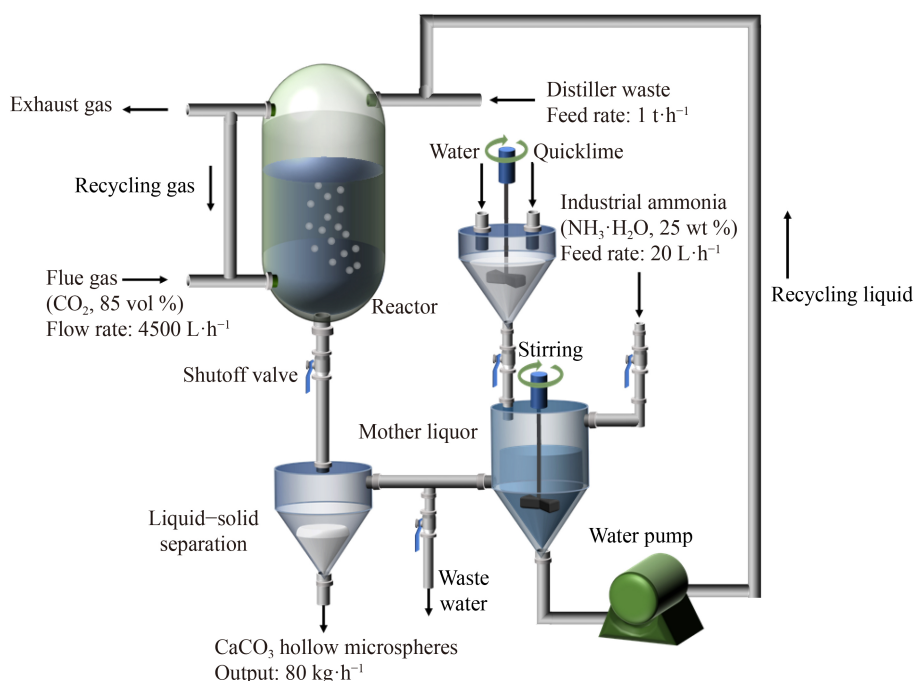


Fig. 10 Flow diagram of CO₂ absorption process by distiller waste.

Table 3 Operational cost analysis of process flow in Fig. 10

Feedstock	Input	Price	Cost estimated per ton distiller waste
Distiller waste	1 t·h ⁻¹	0	0
Flue gas	4.5 m ³ ·h ⁻¹	0	0
Waste ammonia	20 L·h ⁻¹	CNY 2000 per ton	CNY 40
Quicklime	0.8 kg·h ⁻¹	CNY 260 per ton	CNY 0.2
Total			CNY 40.2

Table 4 Profits analysis of process flow in Fig. 10

Product	Output	Price	Yield estimated per ton distiller waste	Profits estimated per ton distiller waste
CaCO ₃ hollow microspheres	80 kg·h ⁻¹	CNY 1500 per ton	CNY 120	CNY 79.8

better explain the process for the formation of hollow microspheres. Besides, it was found that interfacial properties had driven the drastic change from cubic calcite to spherical clusters, since changes in the composition of the solution led to changes in γ_{ls} . This triggered a drastic change in the morphology of the product, corresponding to the changes in surface area of product which in turn was the result of difference between the γ_{ls} and the interfacial energy. Finally, a process for industrial practice was roughly designed and its operational cost was evaluated. Preliminary calculations showed that the operational cost for 1 ton of distiller waste was CNY 40.2, which indicated that the process is profitable if the product price is suitable. Our findings have implications for the high-value utilization of distiller waste and CO₂ from exhaust gas.

Acknowledgements This work is supported by the National Natural Science Foundation of China (Grant Nos. U20A20149, 21878180 and 21908137) and the Graduate Education Project of Shanxi Province (NO. 2021Y139).

Electronic Supplementary Material Supplementary material is available in the online version of this article at <https://dx.doi.org/10.1007/s11705-022-2173-z> and is accessible for authorized users.

Nomenclature

X_V	the molar fractions of vaterite
X_C	the molar fractions of calcite
I_c^{104}	104 crystal plane peak intensities of calcite
I_v^{110}	110 crystal plane peak intensities of vaterite
V_{CO_2}	the total amount of CO ₂ consumed during the carbonation reaction for 1 h, L
V	the volume of solution, L
V_m	the standard molar volume of a gas, L·mol ⁻¹
$n_{Ca(OH)_2}$	the amount of insoluble Ca(OH) ₂ reacted part at time t (negligible), mol
M	molecular weight of Ca(OH) ₂ , g·mol ⁻¹
n	the amount of undissolved Ca(OH) ₂ , mol
$c_{Ca^{2+}}$	the initial concentration of Ca ²⁺ in the solution, mol·L ⁻¹
$c_{Ca^{2+}}$	the concentration of Ca ²⁺ in the solution at time t , mol·L ⁻¹
$c_{Ca^{2+}}$	the concentration of Ca ²⁺ , mol·L ⁻¹
c_{OH^-}	the concentration of OH ⁻ , mol·L ⁻¹
J	the activity products
K	solubility product constant of Ca(OH) ₂ , $K = 5.6 \times 10^{-6}$ (25 °C)

$\gamma_{\text{Ca}^{2+}}$	the activity coefficients of Ca^{2+}
γ_{OH^-}	the activity coefficients of OH^-
$\alpha_{\text{Ca}^{2+}}$	activity of Ca^{2+} in solution, $\text{mol}\cdot\text{L}^{-1}$
α_{OH^-}	activity of OH^- in solution, $\text{mol}\cdot\text{L}^{-1}$
θ	contact angle between calcite and liquid, ($^\circ$)
γ_{ls}	solid–liquid interfacial tension, $\text{mN}\cdot\text{m}^{-1}$
γ_{lg}	liquid–vapor interfacial tension, $\text{mN}\cdot\text{m}^{-1}$
γ_{sg}	solid–vapor interfacial tension, $\text{mN}\cdot\text{m}^{-1}$, $\gamma_{\text{sg}} = 43.5 \text{ mN}\cdot\text{m}^{-1}$
$C_{\text{Ca}^{2+}}^{20\text{min}}$	the concentration of Ca^{2+} in the system reacted for 20 min, $\text{mol}\cdot\text{L}^{-1}$
Y	the output of CaCO_3 hollow microspheres, kg
T	cycle times of carbonation of distiller waste
V'	the volume of distiller waste, L
M'	the molecular weight of CaCO_3 , $\text{g}\cdot\text{mol}^{-1}$

References

- Trypuć M, Białowicz K. CaCO_3 production using liquid waste from Solvay method. *Journal of Cleaner Production*, 2011, 19(6-7): 751–756
- Calban T, Kavci E. Removal of calcium from soda liquid waste containing calcium chloride. *Energy Sources, Part A: Recovery, Utilization, and Environmental Effects*, 2010, 32(5): 407–418
- Sun B C, Wang X M, Chen J M, Chu G W, Chen J F, Shao L. Synthesis of nano- CaCO_3 by simultaneous absorption of CO_2 and NH_3 into CaCl_2 solution in a rotating packed bed. *Chemical Engineering Journal*, 2011, 168(2): 731–736
- Gao C Z, Dong Y, Zhang H J, Zhang J M. Utilization of distiller waste and residual mother liquor to prepare precipitated calcium carbonate. *Journal of Cleaner Production*, 2007, 15(15): 1419–1425
- Zhang X, Asselin E, Li Z. CaCO_3 precipitation kinetics in the system $\text{CaCl}_2\text{--CO}_2\text{--Mg(OH)}_2\text{--H}_2\text{O}$ for comprehensive utilization of soda production wastes. *ACS Sustainable Chemistry & Engineering*, 2020, 9(1): 398–410
- Luo X P, Song X W, Cao Y W, Song L, Bu X Z. Investigation of calcium carbonate synthesized by steamed ammonia liquid waste without use of additives. *RSC Advances*, 2020, 10(13): 7976–7986
- Dong C, Song X, Li Y, Liu C, Chen H, Yu J. Impurity ions effect on CO_2 mineralization via coupled reaction–extraction–crystallization process of CaCl_2 waste liquids. *Journal of CO_2 Utilization*, 2018, 27: 115–128
- Song X W, Liu H, Wang J F, Cao Y W, Luo X P. A study of the effects of NH_4^+ on the fast precipitation of vaterite CaCO_3 formed from steamed ammonia liquid waste and $\text{K}_2\text{CO}_3/\text{Na}_2\text{CO}_3$. *CrystEngComm*, 2021, 23(24): 4284–4300
- Yan Z, Wang Y, Yue H, Liu C, Zhong S, Ma K, Liao W, Tang S, Liang B. Integrated process of monoethanolamine-based CO_2 absorption and CO_2 mineralization with SFGD slag: process simulation and life-cycle assessment of CO_2 emission. *ACS Sustainable Chemistry & Engineering*, 2021, 9(24): 8238–8248
- Alamdari A, Alamdari A, Mowla D. Kinetics of calcium carbonate precipitation through CO_2 absorption from flue gas into distiller waste of soda ash plant. *Journal of Industrial and Engineering Chemistry*, 2014, 20(5): 3480–3486
- Li Y, Song X, Chen G, Sun Z, Xu Y, Yu J. Preparation of calcium carbonate and hydrogen chloride from distiller waste based on reactive extraction–crystallization process. *Chemical Engineering Journal*, 2015, 278: 55–61
- Sha F, Zhu N, Bai Y J, Li Q, Guo B, Zhao T X, Zhang F, Zhang J B. Controllable synthesis of various CaCO_3 morphologies based on a CCUS idea. *ACS Sustainable Chemistry & Engineering*, 2016, 4(6): 3032–3044
- Ma Y, Feng Q, Bourrat X. A novel growth process of calcium carbonate crystals in silk fibroin hydrogel system. *Materials Science and Engineering C*, 2013, 33(4): 2413–2420
- Zheng T W, Zhang X, Yi H H. Spherical vaterite microspheres of calcium carbonate synthesized with poly(acrylic acid) and sodium dodecyl benzene sulfonate. *Journal of Crystal Growth*, 2019, 528(15): 125275
- Chen H G, Leng S L. Rapid synthesis of hollow nano-structured hydroxyapatite microspheres via microwave transformation method using hollow CaCO_3 precursor microspheres. *Ceramics International*, 2015, 41(2): 2209–2213
- Zheng T W, Yi H H, Zhang S Y, Wang C G. Preparation and formation mechanism of calcium carbonate hollow microspheres. *Journal of Crystal Growth*, 2020, 549: 125870
- Wang J, Chen J S, Zong J Y, Zhao D, Li F, Zhuo R X, Cheng S X. Calcium carbonate/carboxymethyl chitosan hybrid microspheres and nanospheres for drug delivery. *Journal of Physical Chemistry C*, 2010, 114(44): 18940–18945
- Park R J, Meldrum F C. Synthesis of single crystals of calcite with complex morphologies. *Advanced Materials*, 2002, 14(16): 1167–1169
- Kim S, Ko J W, Park C B. Bio-inspired mineralization of CO_2 gas to hollow CaCO_3 microspheres and bone hydroxyapatite/polymer composites. *Journal of Materials Chemistry*, 2011, 21(30): 11070–11073
- Yan G W, Huang J H, Zhang J F, Qian C J. Aggregation of hollow CaCO_3 spheres by calcite nanoflakes. *Materials Research Bulletin*, 2008, 43(8-9): 2069–2077
- Hadiko G, Han Y S, Fuji M, Takahashi M. Synthesis of hollow calcium carbonate particles by the bubble templating method. *Materials Letters*, 2005, 59(19-20): 2519–2522
- Tomioka T, Fuji M, Takahashi M, Takai C, Utsuno M. Hollow structure formation mechanism of calcium carbonate particles synthesized by the CO_2 bubbling method. *Crystal Growth & Design*, 2012, 12(2): 771–776
- Yan P, Guo Y P, Xu Z, Wang Z C. Influence of surfactant-polymer complexes on crystallization and aggregation of CaCO_3 . *Chemical Research in Chinese Universities*, 2012, 28(4): 737–742
- Watanabe H, Mizuno Y, Endo T, Wang X W, Fuji M, Takahashi M. Effect of initial pH on formation of hollow calcium carbonate particles by continuous CO_2 gas bubbling into CaCl_2 aqueous solution. *Advanced Powder Technology*, 2009, 20(1): 89–93
- Chen J, Xiang L. Controllable synthesis of calcium carbonate polymorphs at different temperatures. *Powder Technology*, 2009, 189(1): 64–69

26. Wang B, Pan Z H, Du Z P, Cheng H G, Cheng F Q. Effect of impure components in flue gas desulfurization (FGD) gypsum on the generation of polymorph CaCO₃ during carbonation reaction. *Journal of Hazardous Materials*, 2019, 369: 236–243
27. Li E Z, Lu Y, Cheng F Q, Wang X M, Miller J D. Effect of oxidation on the wetting of coal surfaces by water: experimental and molecular dynamics simulation studies. *Physicochemical Problems of Mineral Processing*, 2018, 54(4): 1039–1051
28. Marcolli C. Technical note: fundamental aspects of ice nucleation via pore condensation and freezing including Laplace pressure and growth into macroscopic ice. *Atmospheric Chemistry and Physics*, 2020, 20(5): 3209–3230
29. Cheng H G, Wang X, Wang B, Zhao J, Liu Y, Cheng F Q. Effect of ultrasound on the morphology of the CaCO₃ precipitated from CaSO₄-NH₃-CO₂-H₂O system. *Journal of Crystal Growth*, 2017, 469: 97–105
30. Chen Q J, Ding W J, Sun H J, Peng T J, Ma G H. Utilization of phosphogypsum to prepare high-purity CaCO₃ in the NH₄Cl-NH₄OH-CO₂ system. *ACS Sustainable Chemistry & Engineering*, 2020, 8(31): 11649–11657
31. Cheng H G, Zhang X X, Song H P. Morphological investigation of calcium carbonate during ammonification-carbonization process of low concentration calcium solution. *Journal of Nanomaterials*, 2014, 2014: 1–7
32. Nesbitt H W. Activity coefficients of ions in alkali and alkaline-earth chloride dominated waters including seawater. *Chemical Geology*, 1984, 43(1-2): 127–142
33. Fanghänel T, Neck V, Kim J I. The ion product of H₂O, dissociation constants of H₂CO₃ and Pitzer parameters in the system Na⁺/H⁺/OH⁻/HCO₃⁻/CO₃²⁻/ClO₄⁻/H₂O at 25 °C. *Journal of Solution Chemistry*, 1996, 25(4): 327–343
34. Dean J A. *Lang's Handbook of Chemistry*. New York: The Kingsport Press, 1985: 5–8
35. Li B, Zeng H C. Architecture and preparation of hollow catalytic devices. *Advanced Materials*, 2019, 31(38): 1801104
36. Yang X, Fu J, Jin C, Chen J, Liang C, Wu M, Zhou W. Formation mechanism of CaTiO₃ hollow crystals with different microstructures. *Journal of the American Chemical Society*, 2010, 132(40): 14279–14287
37. Ding W, Hu L, Sheng Z, Dai J, Zhu X, Tang X, Hui Z, Sun Y. Magneto-acceleration of Ostwald ripening in hollow Fe₃O₄ nanospheres. *CrystEngComm*, 2016, 18(33): 6134–6137
38. Weng W, Lin J, Du Y, Ge X, Zhou X, Bao J. Template-free synthesis of metal oxide hollow micro-/nanospheres via Ostwald ripening for lithium-ion batteries. *Journal of Materials Chemistry A: Materials for Energy and Sustainability*, 2018, 6(22): 10168–10175
39. Zhao W, Zhang C, Geng F, Zhuo S, Zhang B. Nanoporous hollow transition metal chalcogenide nanosheets synthesized via the anion-exchange reaction of metal hydroxides with chalcogenide ions. *ACS Nano*, 2014, 8(10): 10909–10919
40. Yin Y D, Rioux R M, Erdonmez C K, Hughes S, Somorjai G A, Alivisatos A P. Formation of hollow nanocrystals through the nanoscale Kirkendall effect. *Science*, 2004, 304(5671): 711–714
41. Fan H J, Gösele U, Zacharias M. Formation of nanotubes and hollow nanoparticles based on Kirkendall and diffusion processes: a review. *Small*, 2007, 3(10): 1660–1671
42. Fan H J, Knez M, Scholz R, Nielsch K, Pippel E, Hesse D, Zacharias M, Gösele U. Monocrystalline spinel nanotube fabrication based on the Kirkendall effect. *Nature Materials*, 2006, 5(8): 627–631
43. Gao J N, Li Q S, Zhao H B, Li L S, Liu C L, Gong Q H, Qi L M. One-pot synthesis of uniform Cu₂O and CuS hollow spheres and their optical limiting properties. *Chemistry of Materials*, 2008, 20(19): 6263–6269
44. Gayevskii V R, Kochmarskii V Z, Gayevska S G. Nucleation and crystal growth of calcium sulfate dihydrate from aqueous solutions: speciation of solution components, kinetics of growth, and interfacial tension. *Journal of Crystal Growth*, 2020, 548: 125844
45. Keller K S, Olsson M H, Yang M, Stipp S L. Adsorption of ethanol and water on calcite: dependence on surface geometry and effect on surface behavior. *Langmuir*, 2015, 31(13): 3847–3853
46. Gao Z, Li C, Sun W, Hu Y. Anisotropic surface properties of calcite: a consideration of surface broken bonds. *Colloids and Surfaces. A, Physicochemical and Engineering Aspects*, 2017, 520: 53–61
47. Tabar M A, Shafiei Y, Shayesteh M, Monfared A D, Ghazanfari M H. Wettability alteration of calcite rock from gas-repellent to gas-wet using a fluorinated nanofluid: a surface analysis study. *Journal of Natural Gas Science and Engineering*, 2020, 83: 103613
48. Ulusoy U, Hiçyılmaz C, Yekeler M. Role of shape properties of calcite and barite particles on apparent hydrophobicity. *Chemical Engineering and Processing*, 2004, 43(8): 1047–1053
49. Chen Z Q. *Colloid and Interface Chemistry*. Peking: Higher Education Press, 2001, 95–104 (In Chinese)
50. Tyson W R, Miller W A. Surface free energies of solid metals: estimation from liquid surface tension measurements. *Surface Science*, 1977, 62(1): 267–276
51. Pan S Y, Chang E E, Chiang P C, Chiang P C. CO₂ capture by accelerated carbonation of alkaline wastes: a review on its principles and applications. *Aerosol and Air Quality Research*, 2012, 12(5): 770–791
52. Ruan J J, Huang J X, Dong L P, Huang Z. Environmentally friendly technology of recovering nickel resources and producing nano-Al₂O₃ from waste metal film resistors. *ACS Sustainable Chemistry & Engineering*, 2017, 5(9): 8234–8240